

# Thermal Diffusivity, Microstructure and Nanohardness of Laser-welded Proton-irradiated Eurofer97

A. P. C. Wylie<sup>a\*</sup>, A. Reza<sup>b</sup>, G. Harrison<sup>c</sup>, M. Taylor<sup>c</sup>, B. R. Dacus<sup>a</sup>, F. Hofmann<sup>b</sup>, M. P. Short<sup>a</sup>, S. Kirk<sup>d</sup>, M. Preuss<sup>c,e</sup>, E. J. Pickering<sup>c,f</sup>

<sup>a</sup>*Department of Nuclear Science and Engineering, Massachusetts Institute of Technology, Cambridge, MA 02139, USA*

<sup>b</sup>*Department of Engineering Science, University of Oxford, Parks Road, Oxford, OX1 3PJ, UK*

<sup>c</sup>*Department of Materials, University of Manchester, Manchester M13 9PL, UK*

<sup>d</sup>*United Kingdom Atomic Energy Authority, Culham Science Centre, Abingdon, OX14 3DB, UK*

<sup>e</sup>*Monash University, Clayton, VIC, 3800, Australia*

<sup>f</sup>*Royce Institute for Advanced Materials, The University of Manchester, Manchester, M13 9PL, UK*

---

## Abstract

Eurofer97 steel, a candidate structural material for future fusion reactors, was examined following 1.9 MeV proton-irradiation up to 0.91(5) dpa at 450 °C with and without a prior post-weld heat-treatment at 760 °C for 4 hours in a laser-welded state. A nanoindentation study found a pile-up-corrected nanohardness of 4.0(4) GPa in the as-welded fusion zone, decreasing to 2.1(3) GPa in the parent material. Irradiation temperature and post-weld heat treatment were both found to have a recovery effect on weld hardness, with the latter being entire. Proton-irradiation damage was not found to contribute to nanohardness at the temperature investigated. X-ray diffraction analysis found increased 1-dimensional dislocation density in the as-welded fusion zone, diminishing to  $3(2) - 19.2(1.4) \times 10^{14} \text{ cm}^{-2}$  in the parent material, dependent on irradiation and heat-treatment. Transient grating spectroscopy of Eurofer97 was attempted, finding a systematic underestimation of thermal diffusivity of average 15.6% from room-temperature to 600 °C when compared to laser flash analysis. Transient grating spectroscopy was, nevertheless, applied determining a room-temperature thermal diffusivity of  $7.8(3) \text{ mm}^2 \text{ s}^{-1}$  in the parent material and  $6.7(4) \text{ mm}^2 \text{ s}^{-1}$  in the as-welded fusion zone. Irradiation at 450 °C alleviated this difference in thermal diffusivity; recovery of weld-induced changes was observed up to 20% in the fusion zone due to irradiation conditions, distinct from temperature effects alone. Such results bode well for Eurofer97's application in fusion reactors, where welding will be essential. Thermal diffusivity has also been mapped at a fine scale across a heterogeneous structure, a technique applicable widely outside the realm of radiation materials science.

**Keywords:** Eurofer97; nanohardness; X-ray diffraction; thermal diffusivity; transient grating spectroscopy; ion-irradiation; low-activation; fusion

---

## 1 Introduction

The conditions present inside deuterium-tritium fusion devices present thermal and radiological materials design challenges to be overcome if economical fusion power is to be achieved. Neutron irradiation campaigns have limitations in terms of time, cost and relevance; no 14.1 MeV neutron source presently exists at the flux necessary to imitate a fusion power plant. Rapid materials innovation in the fusion and fission sectors has compelled radiation materials research towards the cheaper, faster technique of ion-irradiation.<sup>[1]</sup>

Eurofer97 steel has been developed in recent decades as a low-activation structural material for future fusion reactors, featuring extensively in the European plan for a demonstrator fusion reactor.<sup>[2;3;4;5;6;7]</sup> A concerted effort has been made in recent years to identify and optimise welding processes for Eurofer97, with laser-welding presenting clear advantages in terms of deformation,<sup>[8]</sup> porosity,<sup>[9]</sup> and time<sup>[5]</sup> reduction when compared to more traditional joins, such as tungsten inert gas welds. Laser welds exhibit a limited depth of penetration, however, which prevents application to thicker joins more suited to electron-beam welding, though

---

\*Corresponding author: awylie@mit.edu

Table 1: Chemical composition of the material examined in this study. Elements not listed in this table had contributions below 0.02 wt%. Measures were element-specific; a list can be found in the repository provided with this work.

Element	C	Cr	Fe	Mn	Ta	V	W	N <sub>2</sub>
wt%	0.110	9.0	balance	0.52	0.12	0.21	1.1	0.020

Table 2: Laser-welding parameters for Eurofer97 samples.<sup>[10]</sup>

Weld speed	0.5 mm/s
Keyhole laser power	3 kW
Keyhole spot diameter	0.2 mm
Conduction laser power	5 kW
Conduction spot diameter	8 mm

this technique presents challenges around local vacuum requirements. Laser welding can also be useful for remote-maintenance work, as fibre-piped light allows for rapid in-bore cutting and joining of pipes.<sup>[10:5]</sup>

Despite this, the mechanical and thermal properties of laser-welded Eurofer97 in an irradiated state have not yet been investigated in the open literature. Given the general propensity of components to fail at the point of welding, it is critical that such studies be performed if Eurofer97 is to be qualified for reactor use. Not only is Eurofer97 intended as a structural material, but also as breeding and coolant-carrying piping in the reactor blanket;<sup>[11;12]</sup> knowledge around thermal properties evolution with radiation damage is required, in tandem thermal properties can provide insight into the development of radiation damage, as has been demonstrated in more simple materials.<sup>[13;14]</sup> Here is presented a characterisation of laser welded Eurofer97; nanohardness, dislocation density and thermal diffusivity properties for as-welded state and heat-treated welds in both unirradiated and proton-irradiated states. Barring helium production effects, proton irradiation offers comparable radiation damage features to neutron irradiation in the damage ranges considered here,<sup>[1]</sup> with an auxiliary benefit of providing the deepest damage depth for post-irradiation examination. Prior to this work the method used here to probe thermal diffusivity measurements, transient grating spectroscopy (TGS), had limited direct comparisons with traditional thermal diffusivity techniques.<sup>[15;16;17]</sup> TGS has a tuneable depth of investigation, making it an ideal technique for use with the thin damaged layer generated during ion-irradiation. A portion of this work is, therefore, dedicated to the use of this technique in polycrystalline Eurofer97, a ferritic-martensitic steel, using laser-flash analysis as an check of thermal diffusivity.

## 2 Methods

### 2.1 Materials

6 mm thick Eurofer97 plates had been prepared via the standard procedure for the steel:<sup>[18]</sup> hot-rolling, a 30-minute austenitisation at 980°C followed by a rapid quench, then tempered at 760°C for 90 minutes. Autogenously welded plates were received in the as-welded state after having been joined by Kirk et al.;<sup>[10]</sup> a tight keyhole and broad conduction laser weld in tandem allowing for a more stable melt pool. Keyhole laser welding rapidly melts the steel, passing through several phase changes as it heats and cools. The composition and welding parameters of the material are shown in tables 1 and 2, respectively. Before irradiation a portion of the welded plate was sectioned and subjected to a heat treatment of 760°C for 4 hours and air-cooled, a standard post-weld heat-treatment temperature for 9-chrome steels,<sup>[19]</sup> with a view to reduce the impact of freshly formed martensite on weld structural properties. 6x25 mm<sup>2</sup> cross-sections of both the as-welded and heat-treated weld were ground with silicon-carbide pads to a particle size of 3 µm, followed by a diamond paste polish to  $\frac{1}{4}$  µm and mirror finished using 40 nm oxide polishing suspension (OPS). At this stage the fusion zone of the weld could clearly be seen, a more clear depiction of zones in the weld is shown in figure 9.

Table 3: Irradiation parameters and materials preparations for each sample described in this work. Doses listed were averaged over the first 5  $\mu\text{m}$  of the irradiated region.

Sample Number	Heat Treatment	Dose [dpa]	Dose rate [ $\times 10^{-6} \text{ dpa s}^{-1}$ ]	Average ion flux [ $\times 10^{18} \text{ m}^{-2} \text{ s}^{-1}$ ]
0	None	0	0	0
1	None	0.31(2)	2.2(1)	2.04
3	None	0.91(6)	9.92(7)	3.39
4	760°C 4 hrs	0.86(5)	11.6(8)	3.96

## 2.2 Irradiation

Weld sections were irradiated using the BABY accelerator at the Dalton Cumbrian Facility using 1.9 MeV protons at 450°C. A temperature correction, to account for differing dose-rates between protons and neutrons and holding defect recombination rate constant,<sup>[20,21]</sup> shows that this irradiation temperature corresponds to an equivalent neutron irradiation temperature of 418°C. The temperature was chosen as it lays within both temperature estimations for tokamak blanket materials<sup>[22]</sup> and below the temperature at which Eurofer97 tensile properties are observed to degrade.<sup>[23]</sup> Beam current was measured on-stage, sample specific irradiation parameters are displayed in table 3, detailed data on on-stage current is presented in the appendix. Ion-irradiation campaigns are typically performed for Eurofer97 at lower temperatures of around 350°C to better capture the radiation damage before it has annealed. Given welded Eurofer97 has not had the same extensive qualification as the parent material, however, this higher temperature was chosen as the most applicable region for initial study, as annealing effects have a marked impact on weld properties. Samples were mounted on a heating stage with an indium backing applied between sample and stage to provide liquid thermal contact at temperature; monitoring used both a thermocouple welded close to the irradiation region and an infra-red camera. Proton energy was chosen to avoid the  $^{56}\text{Fe}(p,\gamma)^{57}\text{Co}$  reaction, whose onset rises sharply above 1.9 MeV,<sup>[24,25]</sup> and is radiologically undesirable. A gas production calculation was made using the FISPACT-II activation code for the maximum fluence from table 3 and 1.875 MeV protons. No hydrogen production is present while a very low level,  $10^{-4}$  appm, of helium was produced.

Four Eurofer97 samples were irradiated under these conditions: one in the heat-treated state and three in the as-welded. Stopping range of ions in matter (SRIM) is a Monte Carlo based ion-tracking software used to compute displacements per atom (dpa), an estimation of radiation damage based on the average number of times a nucleus has been moved due to incident radiation; calculations were performed for each irradiation using the standard practice of Stoller et al.<sup>[26]</sup> Damage was then averaged across the nanoindentation probe depth of each technique to give the dpa values reported herein. For the 1.9 MeV protons used the Bragg peak of damage occurred  $\approx 18 \mu\text{m}$  from the sample surfaces with the more uniform portion of the damage profile occurring within a depth of 13  $\mu\text{m}$ , shown in figure 1

During irradiation sample surfaces acquired a stained layer on the surface which had to be removed; both TGS and electron microscopy require a fine surface finish, mirrored in the case of TGS. Chemical analysis using energy-dispersive X-ray spectroscopy revealed this was partially due to a fine sputtering of indium covering the surface of the sample. Staining was mostly removed with a diamond paste polish at  $\frac{1}{4} \mu\text{m}$  and mirror finished with OPS, which removed at most 1  $\mu\text{m}$  of material from the surface. See appendix for surface removal study. The remainder of experiments described here were performed in this re-polished state. Non-destructive testing was performed prior to nanoindentation.

## 2.3 Characterisation

Grain size mapping was based on electron backscatter diffraction (EBSD) maps of each polished weld sample. Maps were taken on an FEI Apreo C at a 20 kV accelerating voltage, on-stage current 34.25 nA and a working distance of 25 mm using a Symmetry S2 EBSD detector by Oxford Instruments, step-size 1  $\mu\text{m}$ . Diffraction bands were indexed against an iron body-centred cubic crystallographic database derived from Giles et al.<sup>[28]</sup>

Postprocessing and prior-austenite grain reconstruction used the native Aztec 6.0 and Aztec Crystal 2.2 software packages. Grain-size measurements were taken from the orientation map, raw EBSD pixels were considered within the same grain if they were within an orientation tolerance of 10°. Reconstructions used the

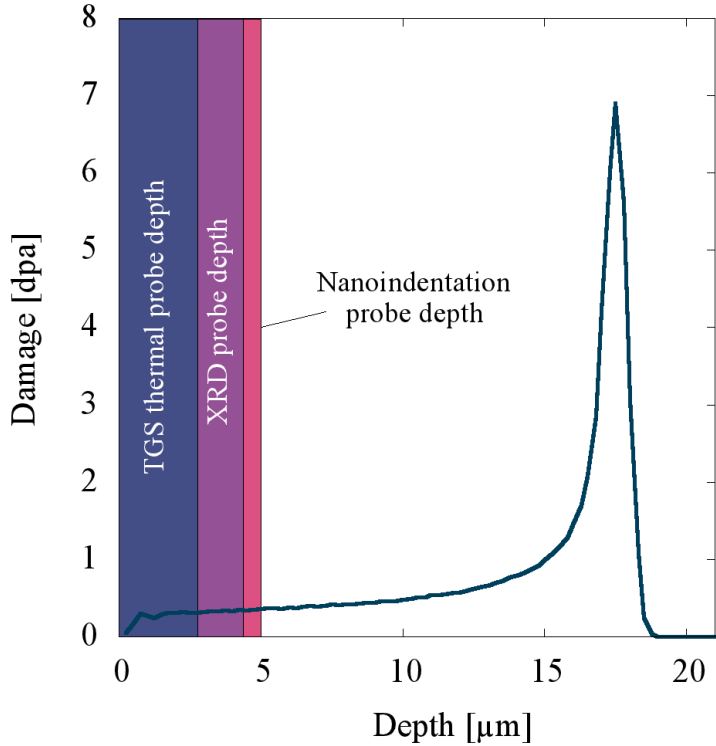


Figure 1: Example SRIM damage profile for 1.9 MeV protons in Eurofer97 for the least damaged irradiated sample in this work. XRD probe depth shown is the maximum possible attenuation depth achieved at normal surface incidence, found using an X-ray penetration tool for elements 1 - 92 developed by Henke et al.<sup>[27]</sup>

Nishiyama-Wassermann crystallographic relations for martensite,  $\alpha'$ , and prior-austenite,  $\gamma$ :

$$\{111\}_\gamma \parallel \{1\bar{1}0\}_{\alpha'} \quad \text{and} \quad \langle\bar{1}01\rangle_\gamma \parallel \langle001\rangle_{\alpha'}. \quad (1)$$

## 2.4 X-ray diffraction

Measurements for X-ray diffraction (XRD) were taken using a Rigaku Smartlab 3 kW. Weld sections were examined in the as-welded state taken to an OPS finish, in the heat treated state and in the irradiated states described previously. One as-welded sample was prepared using electropolishing: taken to an OPS finish and using an electrolyte of 10% perchloric acid in ethanol at -23 °C under a 20 V bias. This left a poor surface finish and so was not attempted for the remainder of samples to allow for TGS and nanoindentation. XRD data from this electropolished sample is, however, presented here.  $2\theta$  sweeps were taken from 40 ° to 120 ° with an X-ray wavelength of 1.54 Å. Sweeps were located in the fusion zone and the parent material of weld sections; spot size was 500 μm. 6 line-profiles were taken for each spot with a 0.01 ° step-size, 0.685 s per step.

Analysis of intensity used the convolutional multiple whole profile (CMWP) fitting package. Diffracted intensity,  $I_{hkl}^{tot}$ , peak broadening was modelled<sup>[29]</sup> as a convolution of crystallite size,  $I_{hkl}^S$ , and strain,  $I_{hkl}^D$ , broadening effects:

$$I_{hkl}^{tot} = I_{hkl}^S * I_{hkl}^D. \quad (2)$$

The broadening terms can be fit to divorce size from strain, size-broadening was evaluated using a least-squared fit to establish crystallite size distribution and has been described thoroughly elsewhere.<sup>[30]</sup> Once isolated, the Fourier-transformed strain-broadening contribution has been shown<sup>[31]</sup> to depend solely on the long-range lattice distortions due to linear defects

$$\mathcal{F}[I_{hkl}^D](L) = \exp(-2\pi^2 L^2 g^2 \langle\epsilon^2\rangle), \quad (3)$$

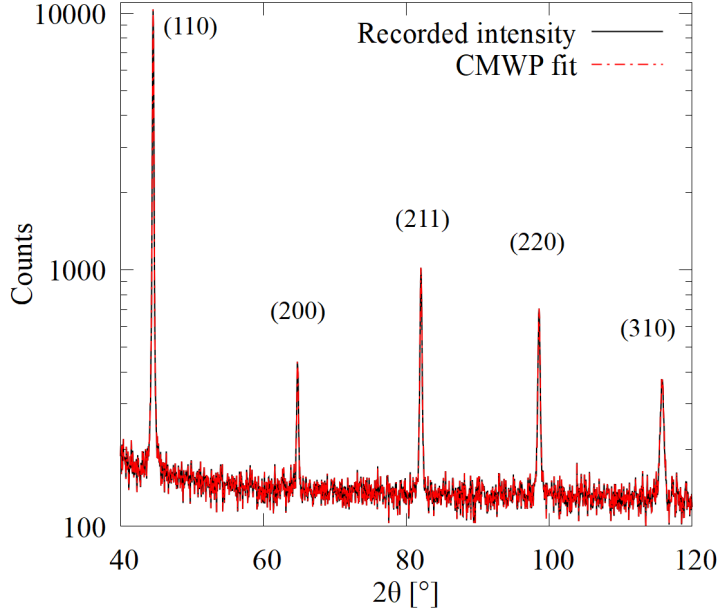


Figure 2: X-ray diffraction  $2\theta$  Eurofer97 parent material sweep (as-welded, OPS finish). Red dashed line represents the nonlinear least squares fit made by the CMWP technique, with counts on a log-scale.

where  $L$  is the Fourier variable,  $g$  the fundamental reciprocal lattice vector and  $\langle \epsilon^2 \rangle$  is the mean square strain, which follows

$$\langle \epsilon^2 \rangle = \frac{\rho C b^2}{4\pi} f\left(\frac{L}{R_e}\right). \quad (4)$$

Here  $f$  is the Wilkens function<sup>[32]</sup> describing the range over which defect strain is felt,  $R_e$  is the effective cut-off radius of that field.  $C$ ,  $b$  and  $\rho$  are the contrast factor, Burgers vector and the density of the dislocations. This calculated intensity is then iterated against the measured by minimising the weighted sum of square residuals (WSSR) between them. Errors for this technique were taken as the range of parameters at which the difference between the WSSR at those parameters and the optimised WSSR would exceed 3.5%. An example fit is shown in figure 2.

## 2.5 Transient Grating Spectroscopy

TGS is a rapid non-contact photothermal technique that can be used to gather thermal and elastic properties of materials to a depth that can be tailored to the needs of the experiment. Such analysis is dearly needed in the field of ion-irradiation science as thin-film materials analysis is often laborious and delicate work.

TGS begins as the interference of two pump laser pulses on a polished sample surface at a known angle. The interference generates an impulse of spatially periodic heating and, therefore, periodic thermal expansion: the transient grating with grating spacing  $\Lambda$ , shown in figure 3. For incident beams, both of wavelength  $\lambda$ , interfering at an inter-beam angle  $\theta$ , grating spacing follows

$$\Lambda = \frac{\lambda}{2 \sin \frac{\theta}{2}} = \frac{2\pi}{q}. \quad (5)$$

$q$  is defined by this relation as the grating wavenumber. This temperature and displacement field set up a surface acoustic wave (SAW) whose decay is then monitored using a probe and reference beam, diffracted from the grating and collected in a dual-heterodyne configuration.<sup>[33]</sup> The surface displacement temporal response of this periodic impulse has been shown to follow the complementary error function in time,<sup>[34]</sup> while surface temperature evolves as a radical-attenuated exponential decay. Combined, these terms form the theoretical basis for transient grating response,  $I_P$ :<sup>[34]</sup>

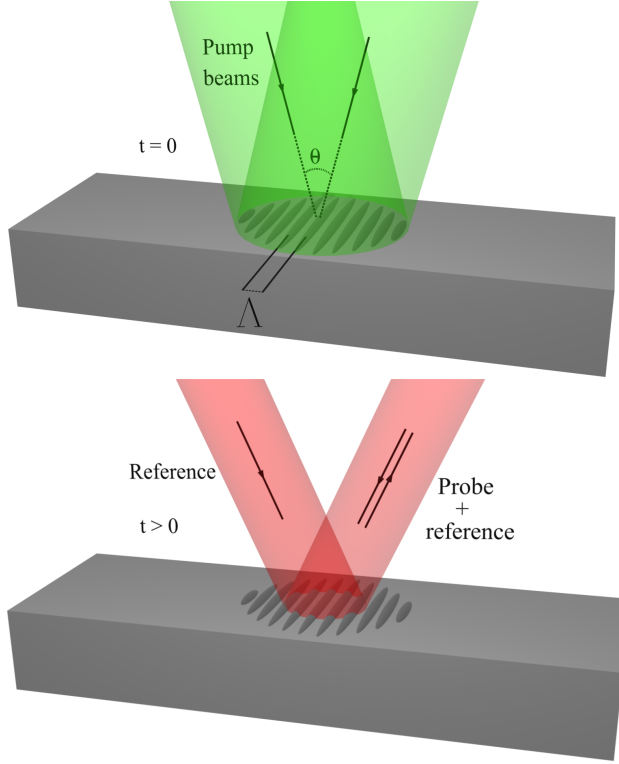


Figure 3: The process at the core of TGS: a transient grating formed via two pump lasers interfering at an angle  $\theta$ , top, and its decay monitored by a probe beam, bottom.

$$I_P(t) = A \left[ \text{erfc}(q \sqrt{\alpha t}) - \frac{\beta}{\sqrt{t}} e^{-q^2 \alpha t} \right] + B \sin(2\pi f t + \Theta) e^{-\frac{t}{\tau}} + C, \quad (6)$$

where  $A$ ,  $B$  &  $C$  are fitting constants,  $\beta$  represents the ratio of contributions to the signal from displacement and reflectivity,  $f$  is SAW frequency,  $\Theta$  is acoustic phase and  $\tau$  is the acoustic decay constant.<sup>[35]</sup> The additional sinusoid accounts for acoustic oscillations that can be seen in figure 5, and reduces errors brought about by fit-start variation.

Critically, TGS has a tailorabile depth of investigation<sup>[17]</sup> for thermal properties,  $L_{th}$ , where

$$L_{th} = \frac{\Delta}{\pi}. \quad (7)$$

By varying the angle of pump incidence,  $\theta$ , these depths can be adjusted, suitable to the thickness of the irradiated layer in question. This depth represents the distance from the surface at which thermal contributions to the transient grating decay are reduced to a factor of  $\frac{1}{e}$  when compared to at-surface contributions.

Two separate TGS apparatus were used in the present work, the first (TGS A) of which was used for a temperature ranged diffusivity study of as-welded Eurofer. A 532 nm pump laser was used, repeating at 1 kHz, along with a 785 nm quasi-continuous beam also made to pulse at 1 kHz using a chopper wheel and beam-split to form the two probe beams to be heterodyned. Pump and probe beams were passed through a grating of nominal spacing 6.4  $\mu\text{m}$  and the first-orders converged on a polished Eurofer97 surface, in a vacuum chamber, to form the transient grating in a manner described in figures 3 & 4. Grating spacing at the sample was calibrated using SAW frequency in single-crystal tungsten, which has a SAW speed of 2669.5  $\text{m s}^{-1}$ ,<sup>[36]</sup> to be 6.457(2)  $\mu\text{m}$ .

Probe beams were collected in two Si-avalanche photodiodes, band between 50 kHz – 1 GHz (3 dB). Collected signals had their phase maximised oppositely using probe phase adjusters and the difference taken as the TGS signal, shown in figure 5. Oppositely maximised signals select the inter-probe phase difference of  $\pm\frac{\pi}{2}$  and eliminate the need to investigate the precise phase difference. This antiphase arrangement has been shown to

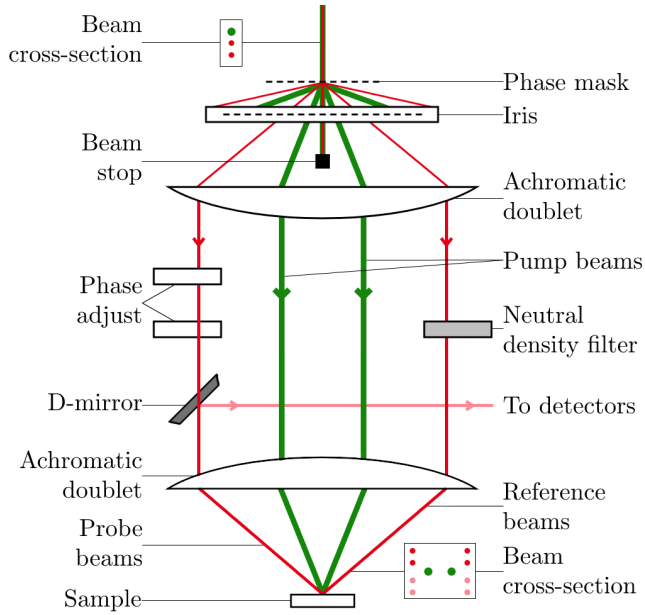


Figure 4: Schematic showing the construction of dual-heterodyne TGS conditions. 1 kHz pulsed beams enter at the top and two output signals are collected to the right. Sample was contained within a vacuum chamber, omitted here for clarity.

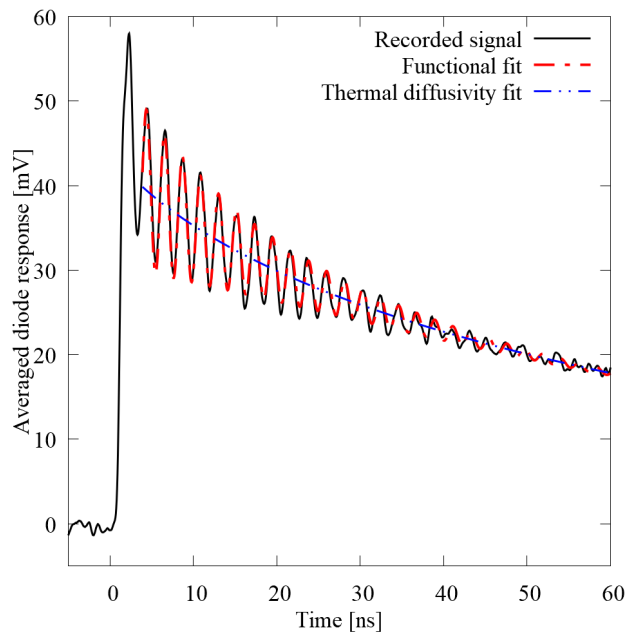


Figure 5: Example TGS signal for Eurofer97 parent material, truncated; measurement window for each signal was 500 ns. The full fit of equation 6 is in red. The thermally governed grating decay is described by the blue line, representing the fit without the acoustic term.

be stable against small changes in phase.<sup>[13]</sup> Each final output signal was averaged over 10,000 pulses and a no-signal reading subtracted to minimise noise.

Measured SAW decay was then fitted using iterative parameter estimation fed into a nonlinear least squares calculation<sup>[13]</sup> to find the parameters contained in equation 6, notably thermal diffusivity. Errors were taken at a 95% fit confidence interval. For TGS A this fitting started at the second SAW oscillation, as shown in figure 5 so to exclude the singular point  $t = 0$  in equation 6. For TGS B this fitting was averaged, using the first 5 SAW peaks as starting points.

The second TGS arrangement (TGS B) was similar to the first and used the same 532 nm wavelength pump beam but a 559.5 nm wavelength probe, both at a 1 kHz repetition rate at a 8.733(2)  $\mu\text{m}$  tungsten-calibrated grating spacing. This grating implies a theoretical depth of investigation of 2.7797(6)  $\mu\text{m}$  for thermal properties. The vacuum chamber for this system was mounted on a stage, capable of moving in a plane normal to the beam axis and used to map irradiated welds precisely. To compensate for sample unevenness a plano-convex mirror was placed in front of each of the detectors (of similar specifications to those previously mentioned) which have been shown to allow for up to  $1.5^\circ - 2^\circ$  surface tilt, depending on rotation axis.<sup>[14]</sup> A dichroic mirror (505 nm cutoff), used for sample microscope observations, was positioned immediately outside the vacuum chamber and has been shown to have no effect on TGS readings.<sup>[14]</sup> Other than the differences listed here, the two TGS systems were the same.

Post-irradiation, samples were mapped with TGS B, in vacuum, at 250  $\mu\text{m}$  intervals in the horizontal and vertical direction from the weld centre to the sample edge, spanning the 6 mm height of the weld sections. Each point sampled had a spot-size of 90  $\mu\text{m}$  for probe and 140  $\mu\text{m}$  for pump beams (taken at intensity reduction  $\frac{1}{e^2}$ ) which is large enough to sample multiple grains per spot. Signals were then fit, again using a nonlinear least squares method, to equation 6 without the thermally induced reflectance term to extract thermal diffusivity values. The value of  $\beta$  in equation 6 was found to typically be of order  $10^{-6} \text{ s}^{\frac{1}{2}}$  in Eurofer97 and so can safely be neglected, indicating that the physical grating generated by thermal expansion contributes far more strongly than that due to thermally induced changes in reflectivity.

The assessment of crystallographic orientation of single-crystals in TGS work is a key prelude impossible to perform here. Establishing the directions along which SAWs, pseudo-SAWs and bulk waves propagate is typically required, where SAW direction is found at lowest acoustic frequency. The formation of equation 6 does not account for the behaviour of pseudo-SAWs and bulk waves, which radiate energy from the surface, rather than along it. Consequently, TGS-gotten thermal diffusivity in polycrystals may include contributions from these bulk-radiative waves. A further discussion of this challenge is presented along with the results.

## 2.6 Laser Flash Analysis

A validation study for Eurofer97 using laser flash analysis (LFA) was taken with a Netzch LFA 427. Weld regions tested were the parent material and the fusion zone; two samples were cut from the as-welded plate using electronic discharge machining to create cylinders, height 2 mm and radius 6 mm and carbon spray-coated to provide a photoabsorptive layer. A solid-state 1064 nm laser deposited a 25 J pulse on one flat side of the sample in an argon atmosphere; temperature rise was monitored on the opposite face with an infra-red camera. Five shots were taken at each temperature step.

Half point in temperature rise-time,  $t_{1/2}$ , then established the thermal diffusivity,  $\alpha$  for the shot as<sup>[37]</sup>

$$\alpha = 0.1388 \frac{L^2}{t_{1/2}}. \quad (8)$$

Sample thickness,  $L$ , for the current work was the cylinder height and was measured precisely for each sample. A total of 5 shots were taken for each temperature point; temperature was ranged from room temperature and then 50-600°C at 50°C intervals.

It should be noted that the fusion zone in the Eurofer97 welds studied, at its thinnest, is around 1.5 mm wide, as can be seen in figure 9. The 2 mm tall cylinders necessarily sampled a partial volume of the heat-affected zone (HAZ).

## 2.7 Nanoindentation

1  $\mu\text{m}$  fixed-depth quasi-static indents were performed for each sample on the Hysitron TI 980 nanoindenter equipped with a diamond Berkovich tip in line with the method set out by Oliver & Pharr.<sup>[38]</sup> For this depth

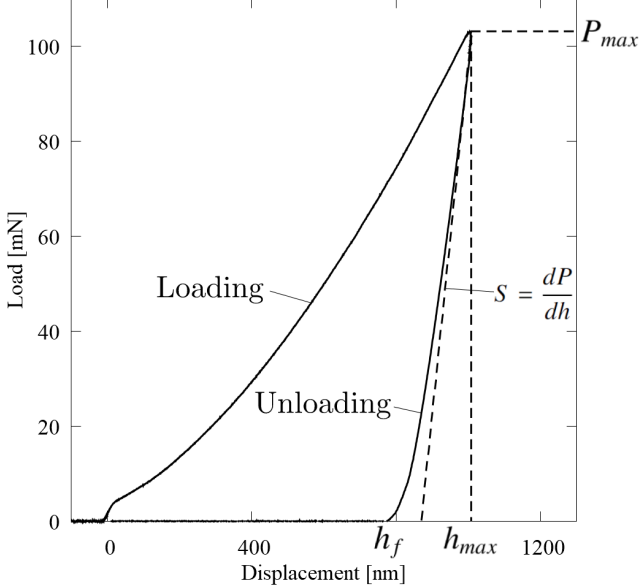


Figure 6: Typical load-displacement curve for Eurofer97 in the unirradiated fusion zone.

of indent the extent of the plastic zone is shown in figure 1 in pink. Indents were spaced at 250  $\mu\text{m}$  in both horizontal and vertical directions.

Hardness,  $H$ , is calculated from the load-displacement curve (see figure 6 for example curve used in this work) using the maximum load,  $P_{max}$ , and the inferred projected contact area,  $A_i$ , as

$$H = \frac{P_{max}}{A_i}. \quad (9)$$

$A_i$  is calculated assuming that all plastic deformation caused by the indent occurs into the sample, the area is taken as the cross section of the Berkovich tip at the inferred contact height,  $h_c$ , via the tip inferred projected contact area function

$$A_i(h_c) = C_0 h_c^2 + C_1 h_c + C_2 h_c^{\frac{1}{2}} + C_3 h_c^{\frac{1}{4}}. \quad (10)$$

Coefficients for this function are tip-specific and were calibrated using a fused silica reference sample:  $C_0 = 24.5$ ,  $C_1 = 6203.49 \text{ nm}$ ,  $C_2 = -157195 \text{ nm}^{\frac{3}{2}}$ ,  $C_3 = 429829 \text{ nm}^{\frac{7}{4}}$ . Inferred contact height is calculated via the load-displacement curve

$$h_c = h_{max} - \epsilon \frac{P_{max}}{S}. \quad (11)$$

Here  $h_{max}$  is the depth at maximum load,  $S$  the stiffness calculated as the initial gradient of the unloading curve and  $\epsilon$  a tip geometry factor taken as 0.75. However, the assumption of in-sample plasticity does not always hold, as is the case in the present work where indent pile-up can affect results: underestimating the area of contact with the indenter overestimates hardness.

Indent images taken in a scanning electron microscope (SEM) revealed a systematic underestimation of the inferred projected contact area of indents by between 16 – 30 %, based on location within the weld, see appendix for data. A correction factor could be formed, based on the ratio of the imaged triangular area to the inferred, but this correction would be superseded by a subsequent pile-up correction. Examples of these measured areas are shown in figure 7. Nanoindents easily fulfilled the condition required for pile-up,  $\frac{h_f}{h_{max}} > 0.7$ ,<sup>[39]</sup> where  $h_f$  is the final indenter depth as load is reduced to 0; in Eurofer97 this ratio is around 0.9 in both parent and welded material at both irradiated and unirradiated states. A portion of indents were, therefore, examined using a SEM to evaluate the extent of pile-up effects. To rectify, a correction term in both the weld region and the parent for pile-up effects in Eurofer97 nanohardness,  $H_{corr}$ , was found, of the form

$$H_{corr} = \frac{A_i}{A_c} H_N = A_{corr} H_N. \quad (12)$$

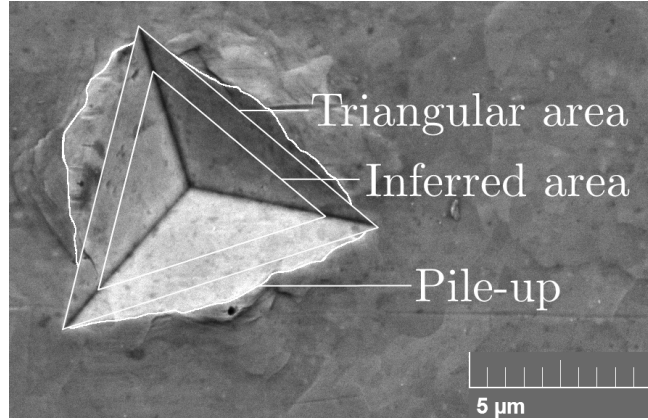


Figure 7: SEM image of a  $1 \mu\text{m}$  indent in  $0.31(2)$  dpa proton-irradiated Eurofer97 showing the three areas discussed.

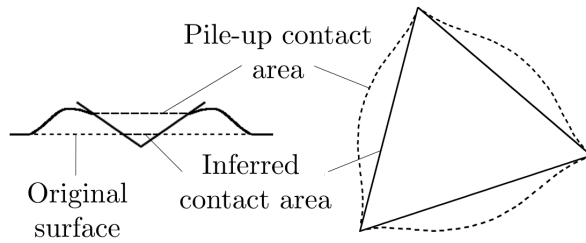


Figure 8: Schematic showing a side- and a top-view of a piled-up Berkovich-tip indent showing inferred contact area,  $A_i$ , and pile-up contact area,  $A_c$ .

Here  $A_c$  is pile-up contact area and is the surface-projected area of the region of contact with the indenter tip, shown in figure 8. This correction term was calibrated averaging over 57 nanoindent images spanning from the parent material to the fusion zone and measuring the pile-up area using the ImageJ software package, finding  $A_{corr} = 0.6922$  in the parent and  $A_{corr} = 0.6712$  in the weld. Additionally, a measure of the nanoindenter machine compliance was made using a fused silica standard, and was found not to impact results, see appendix for study.

### 3 Results and Analysis

#### 3.1 Characterisation

A crystallographic orientation map of an as-welded Eurofer97 section can be seen in figure 9, showing the alignment of ferrite grains. Starting on the left from the fusion zone, the characteristic columnar austenite solidification along the direction of heat flow in the weld can be seen bordered by a thin layer of coarse grains, identified as weld-induced coarse-grained austenite at the border of the fusion zone (the coarse-grained HAZ). As these austenite regions cooled they transformed back to martensite. A strip of what was fine-grained austenite are visible immediately adjacent; these austenite grains also fully transformed back into ferritic-martensitic Eurofer97 post-weld (the fine-grained HAZ). A tempering effect is then observable as temperatures in the weld at this inter-critical position failed to reach the  $\text{Ac}_3$  of around  $890^\circ\text{C}$ .<sup>[40]</sup> grain growth is apparent in the equivalent circle diameter (ECD) grain size mapped from weld centre out, figure 10a. ECD here represents the grain cross sectional area converted to be circular, with its diameter taken as the measure of grain size. The result is a mixed microstructure of over-tempered ferrite and fresh austenite. Prior-austenite grain reconstruction may not be suitable in the intercritical grain growth region in the HAZ due to the mix of microstructural changes present.

Continuing right, the over-tempered region then transitions to the parent material with its refined grains. Figure 10a shows this profile of coarsest-fine-coarser-fine in the unreconstructed data clearly. Irradiation and heat-treatment appear to have little effect on grain size for the samples studied in this work. Maps shown are

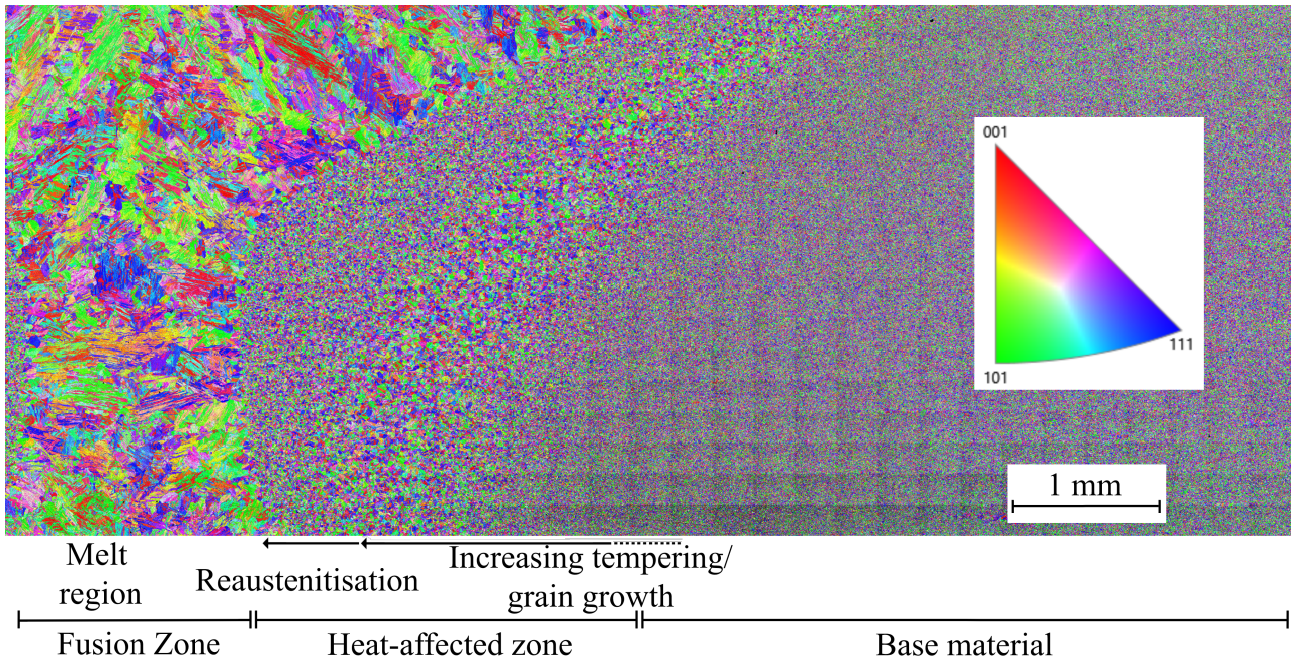


Figure 9: EBSD montage of as-welded Eurofer97 showing ferrite grains without PAGS-reconstruction with inverse pole-figure y-alignment (IPF Y) colouring. Some stitching artefacts remain in the parent material where very fine grain sizes are present.

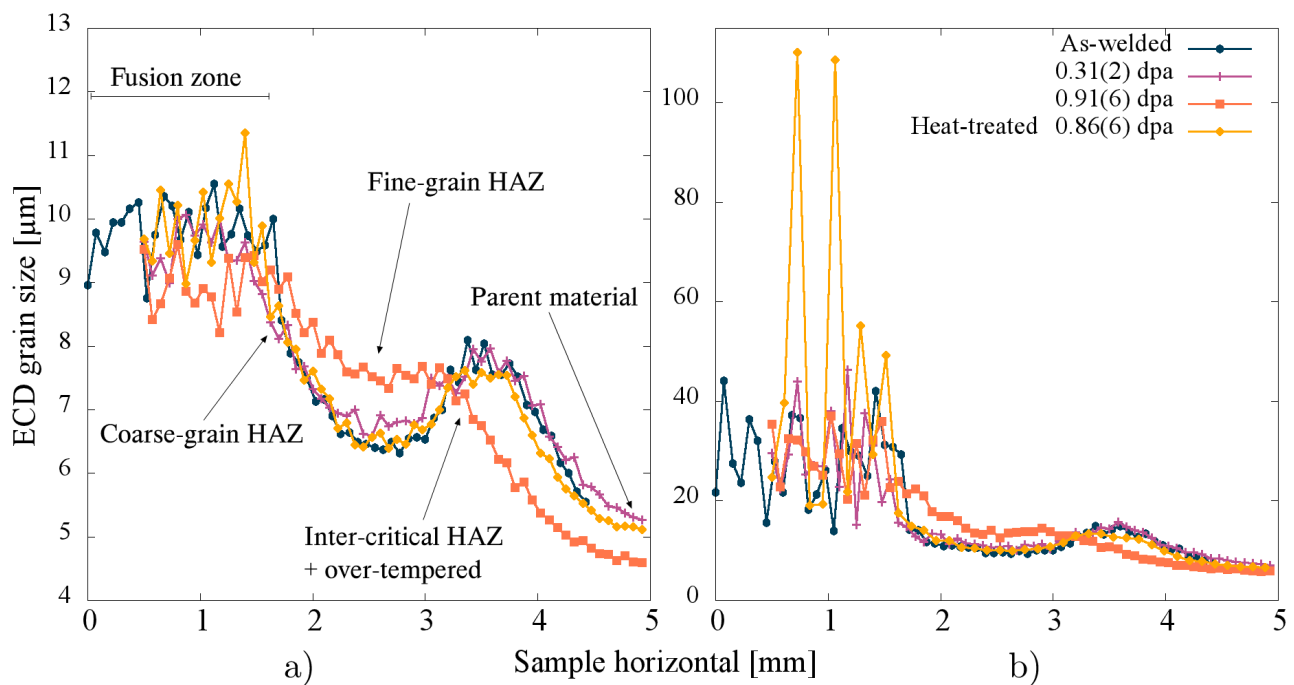


Figure 10: Average ECD grain size for Eurofer97 samples examined in this work taken along the central strip of each map (the irradiated region for those samples irradiated). Left is the raw EBSD-measured ferritic grain size and right the prior-austenite reconstructions. Scans range from the weld centre, at 0.5 mm along the sample horizontal, to the parent at 5 mm.

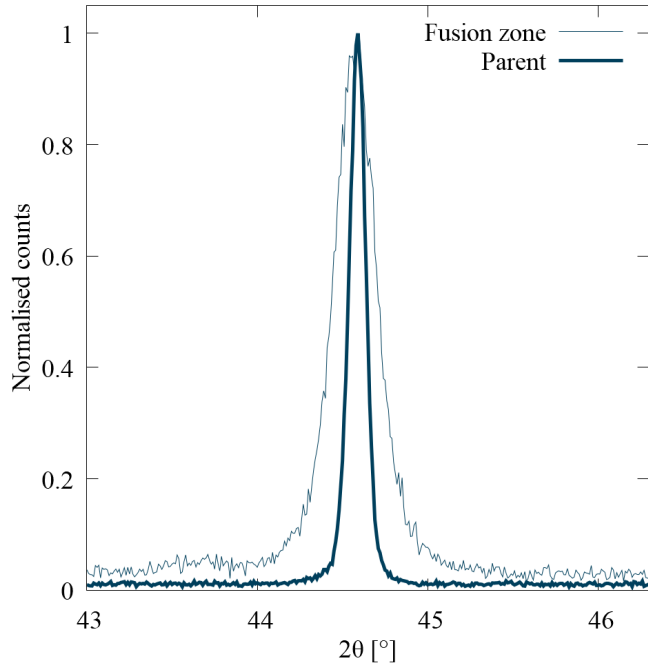


Figure 11: XRD intensity readings for the (110) peak in as-welded Eurofer97 for parent and fusion zone, normalised by respective maximum intensities.

very similar in features, with differences between them likely due to fluctuations in the shape of the melt pool during the welding process.

Prior-austenite grain reconstructions revealed maps near-identical in trend to the unreconstructed for each sample, shown in figure 10b. The two high points present in the heat-treated fusion zone can be traced to two large grains found in the weld region of the 0.86(6) dpa sample. Within the fusion zone the large grain size precludes a high number of grains from being sampled in the mean, large grains such as these will, therefore, self-weight in averages presented. Putting these two outliers aside, treatments in this work do not have an effect on prior-austenite grain size as would be expected from the temperature ranges investigated.

### 3.2 X-ray Diffraction

An example XRD peak broadening difference between the Eurofer97 weld and parent material can be seen in figure 11, where as-formed martensite exhibits distinct broadening when compared to the tempered parent. Shown in figure 12, the dislocation density was found for the fusion zone and the parent material for each sample studied here. The two reference points were taken from the unirradiated regions in irradiated samples; the first in the irradiated heat-treated sample, the other was taken from a failed Eurofer97 sample that spent 8 hours in the beam target at 450 °C.

Dislocation density in the as-welded fusion zone is high when compared to the tempered parent material; the as-quenched martensite naturally has a high dislocation density and high internal stresses.<sup>[41;42]</sup> As shown in later nanohardness data, this results in a high nanohardness despite a high grain size in this region.

Post-weld heat-treatment at 760 °C led to a reduction in fusion zone dislocation density. Given the post-weld heat treatment of 4 hours was at the same temperature to that of the parent tempering step (760 °C for 90 minutes), the dislocation density of the heat-treated fusion zone in figure 12 approaches that of the as-welded parent material, as the types of dislocations whose migration is activated will be the same at these temperatures. Internal stresses seek to relax and do so at these elevated temperatures, migrating dislocations to grain boundaries or other higher-dimensional aggregates not observable using CMWP fitting. This result is corroborated by a recent study of laser-welded Eurofer97, heat-treated at the same temperature for 90 minutes, finding a 90% drop in weld internal stress.<sup>[43]</sup> The heat treatment of the irradiation has similar effects to post-weld heat treatment. The electropolished results in each region are lower than in the OPS-polished state, though in the fusion zone dislocation density remains high.

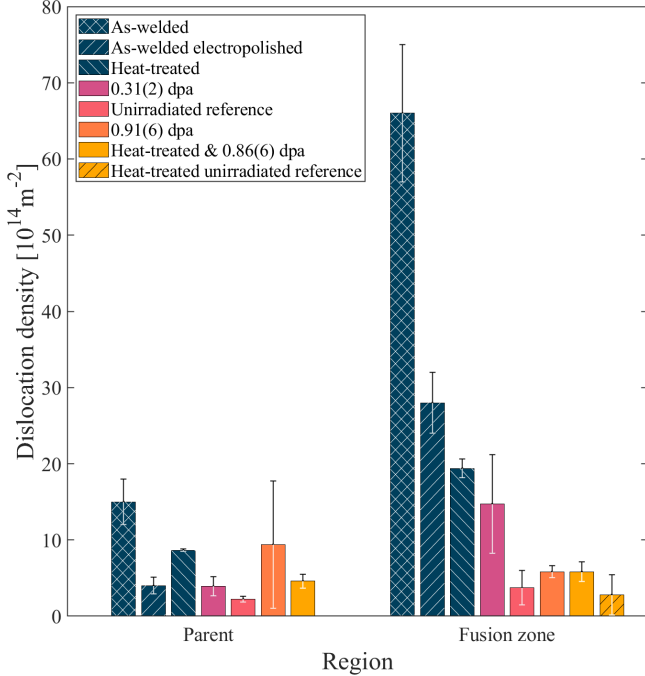


Figure 12: Dislocation density outputs from CMWP fits for each of the samples examined in the present work. Points labelled “reference” were taken from irradiated samples in regions that were blocked off from the ion beam, and so have a similar thermal history. Horizontal spread around the two zone axis labels is for visual clarity only.

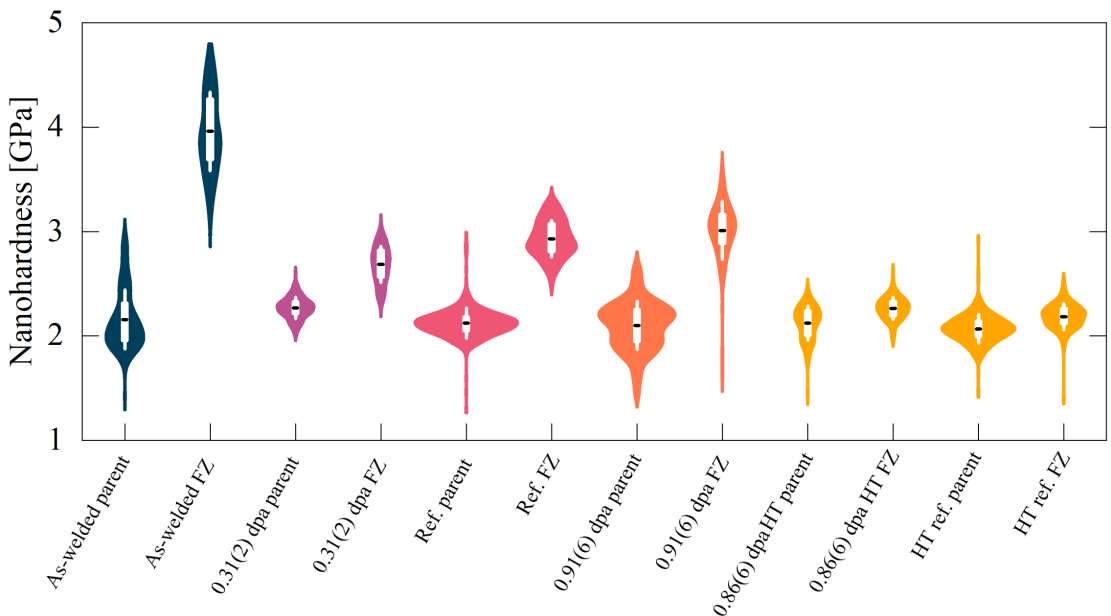


Figure 13: Violin plots of pile-up-corrected nanohardness for the Eurofer97 samples studied in the parent and fusion zone (FZ) in the irradiated cases and the heat-treated then irradiated cases. White boxes represent the inter-quartile range containing the mean black bar, whiskers represent a standard deviation. Distributions of datasets for each sample, of the order of hundreds of indents, are displayed symmetrically as wings and are scaled according to the size of each dataset. Reference sample underwent similar heat-treatment and post-irradiation polishing to those irradiated, but without irradiation.

### 3.3 Nanoindentation

Figure 13 displays the pile-up corrected nanohardness data for this work. Starting in the as-welded condition there is a marked increase in nanohardness in the fusion zone, as would be expected in as-formed martensite and in agreement with increases reported for microhardness in laser-welded Eurofer97.<sup>[10;41]</sup> Errors here are dominated by point-to-point variation. As indicated by the XRD results of this work, there is a degree of dislocation hardening present in the as-welded fusion zone when compared to the tempered parent. The irradiation temperature of 450 °C alone brings fusion zone nanohardness down from 4.0(4) to 2.9(2) GPa, a recovery of 28%. Unlike the thermal diffusivity and dislocation density data of this work there is not a complete recovery to levels found in the parent material, at 2.2(4) GPa, indicating the hardening mechanisms in the weld are not solely due to dislocation damage observable with prior techniques.

Proton-irradiation at temperature appears to leave the parent material nanohardness unaffected, data from the irradiated samples with and without heat-treatment are close to identical. An extended holding time at the irradiation temperature consistently reduces the nanohardness in the fusion zone to a similar level, indicating the recovery that is possible at 450 °C completed in all samples irradiated. At the higher heat-treatment temperature of 760 °C nanohardness entirely recovers to the level of the unirradiated parent material.

### 3.4 Thermal Diffusivity

Figure 14 shows a comparison between the two techniques used to obtain thermal diffusivity in this work, errors presented with LFA represent the standard deviation of data for each temperature point. LFA data from the present work closely match existing LFA data in parent Eurofer97. There is some discrepancy at lower temperature, however, historical data was not presented with detailed errors, and so the extent of the disagreement cannot be fully explored. Fusion zone thermal diffusivity is lower than that in the parent across all temperatures which is in line with reasoning around dislocation density. Freshly formed martensite formed in the fusion zone contains within it many more sites for electrons to scatter from. Fusion zone and parent thermal diffusivities converge at higher measurement temperatures in both TGS and LFA, martensite tempering is observable at these elevated temperatures.

TGS thermal diffusivity temperature variation readings were made using TGS A. Deviation between measured thermal diffusivity in Eurofer97 at room temperature between TGS A and TGS B was below 0.9 %. TGS systematically underestimates the thermal diffusivity of the steel across the temperature range examined by an average of 15.6%. Despite this shift the difference in measured diffusivity between parent and fusion zone is the same for TGS and LFA, to within error, across the temperature range for which it is measurable, confirming that the shift is systematic.

A TGS linescan average was taken from weld centre to edge in each of the samples studied in this work. Shown in figure 15, a clear distinction can be made between the parent, at 7.8(3) mm<sup>2</sup> s<sup>-1</sup>, and weld region, at 6.7(4) mm<sup>2</sup> s<sup>-1</sup>, in the as-welded condition. Fit errors, as stated in the methods section, were taken at a 95% confidence interval. Overall errors, however, were dominated by point-to-point spread. This same point-to-point effect is observed in single crystal materials and may be due to slight changes in microstructure from point-to-point as is virtually impossible to achieve defect-free crystals. In steel there is the added complication of grains, subgrains, carbides and solid solution contributions to this thermal diffusivity and the transient grating phenomenon. The spot size for these maps (TGS B) was 140 µm for the pumps and 90 µm for the probes, taken at a reduction to  $\frac{1}{e^2}$  of central value.

In all irradiated conditions the transition between parent and weld is not as sharp as it is in the unirradiated, and so a change in relation to the unirradiated portion of each sample was also calculated, shown in figure 16. In the as-welded samples there is no discernible difference between the unirradiated and irradiated parent material. In the weld region and the HAZ, however, a slight recovery effect is present, also shown in figure 16, improving thermal diffusivity in the region by up to 20% and bringing it in line with the parent material.

## 4 Discussion

### 4.1 Characterisation

There is an interaction of weld-induced heating and existing microstructure present in the HAZ, where a mixture of reaustenitisation and grain growth occurs. To be clear, there is evident ferrite grain growth happening due to elevated temperature having its own historic prior-austenite grain size altered. In addition, the partial new

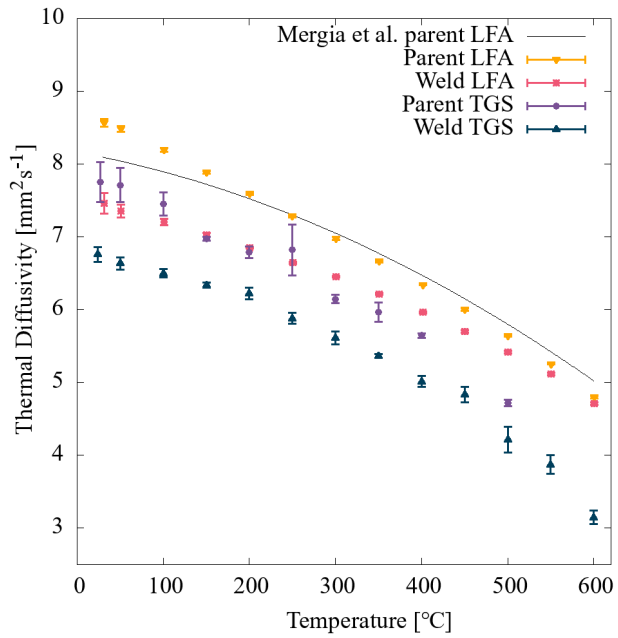


Figure 14: Thermal diffusivity values for Eurofer97 in the parent material taken using LFA and TGS from room temperature to 600 °C. Literature curve after Mergia et al.<sup>[44]</sup>

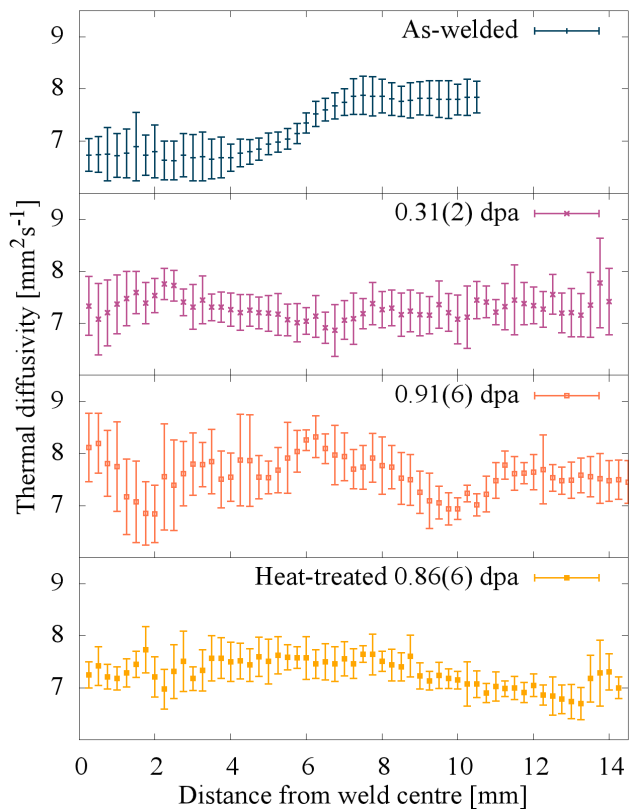


Figure 15: Thermal diffusivity linescans in the irradiated regions within of each sample examined.

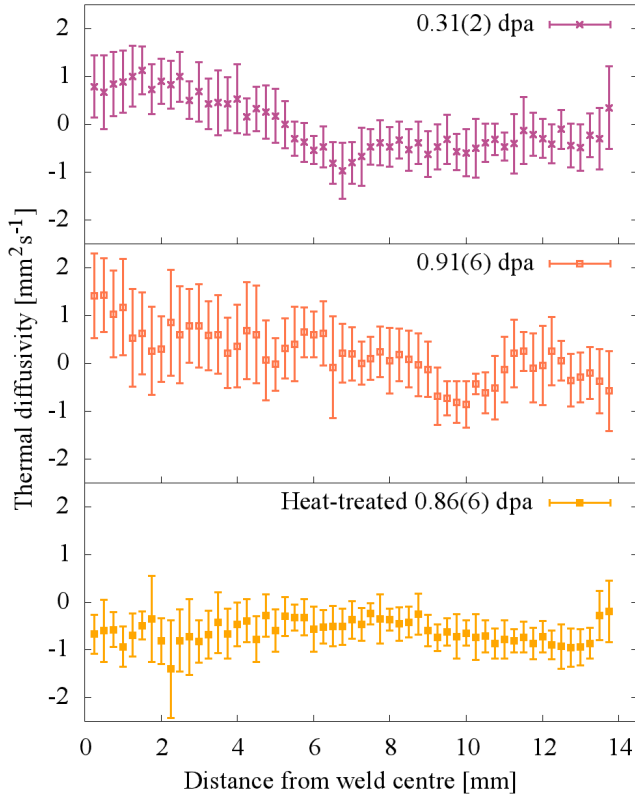


Figure 16: Difference in thermal diffusivity between irradiated and unirradiated regions within each of the irradiated samples examined.

re-austenitisation of grains in this region will give a finer reading for grain size, resulting in a mixed population of coarse- and fine-grains. This does not detract from the lack of radiation effects on grain distributions, though it should be noted when considering absolute grain sizes reported here.

## 4.2 X-ray Diffraction

A recent paper by Stornelli et al.<sup>[45]</sup> investigates the dislocation density in Eurofer97 using X-ray line-profile analysis, not using CMWP, finding the dislocation density of  $8 \times 10^{14} \text{ m}^{-2}$  compared to  $15(8) \times 10^{14} \text{ m}^{-2}$  in the present work. Errors are not presented, however, and so a comparison is difficult. These densities are consistent with results reported for other martensitic steels. Studies of both as-quenched<sup>[46]</sup> and tempered<sup>[42;47]</sup> martensites (with varied chemical compositions) have recently reported 1-dimensional defect densities of around  $40 \times 10^{14} \text{ m}^{-2}$  and  $2 - 4 \times 10^{14} \text{ m}^{-2}$ , respectively, serving as order of magnitude checks for results reported here.

Of note is the electropolished sample in this study. Electropolishing removes surface stresses, and, therefore, dislocations, arising from mechanical polishing and when compared to the mechanically polished as-welded sample there is a sharp decrease observed, though the dislocation density remains high. While this reveals that the dislocation legacy of martensite formation is not quite so large, overall trends of high density in the fusion zone to lower in the parent remain.

Holding as-welded Eurofer97 at the operating temperature of  $450^\circ\text{C}$  appears to generate a similar result (in terms of nanohardness change) to the  $760^\circ\text{C}$  heat-treatment. Recovery at this temperature is common in martensitic steels;<sup>[41]</sup> a partial recovery of tensile and hardness properties in highly work-hardened Eurofer97 has been observed after a heat-treatment at  $450^\circ\text{C}$  for 1 hour.<sup>[45]</sup> The period of irradiation for samples in the current work ranged from 20 – 40 hours, with the reference sample (pink in figure 12) having been held for 8 hours in the sample conditions. It is likely that treating at this longer time-frame allows for greater recovery. A vacuum annealing study at  $450^\circ\text{C}$  with varied durations would establish the validity of this statement; between 9 and 40 hours the effects of 1-dimensional defect annealing have already saturated to the levels present in the heat-treated samples.

Among the unirradiated reference samples and the irradiated there is little difference in measured defect density between the fusion zone and parent material. Resistivity recovery experiments with proton-irradiated

Eurofer97 have established the irradiation-induced dislocation migration-onset temperatures,<sup>[48]</sup> finding the highest, before complete recovery, to be at 327 °C. Above this temperature, defects from proton-induced cascades that contribute to electronic scattering are being completely annealed out. While it is flawed to assert now the same is happening here, this is a possible explanation as to the lack of radiation-induced linear defects within the samples in this report. Future experiments to determine electronic scattering rates of the defect types in Eurofer97 would link these two findings and lend weight to this reasoning. Aside from resistivity, studies of parent Eurofer97 have shown almost comprehensive recovery of irradiation induced changes of microhardness,<sup>[49]</sup> ductility and tensile strength<sup>[50]</sup> in proton- and neutron-irradiations following a post-irradiation hold at 450 °C.

### 4.3 Nanohardness

The freshly formed martensite in the fusion zone likely has a higher degree of substitutional solid solution strengthening when compared to the tempered parent,<sup>[41]</sup> given the diffusionless nature of the martensitic transformation. The discrepancy between the fusion zone nanohardness in the sample heat-treated at 760 °C (yellow) before the 450 °C irradiation and those not (other colours), seen in figure 13, may be due to the retention of these alloying elements in solid solution, such as the carbide-forming chromium and vanadium. This hypothesis could be tested as part of the vacuum annealing study proposed in the XRD section of this work, using transmission electron microscopy to establish any changes in carbide size after heat-treatments at varying temperatures. Were it correct, at some critical temperature between 450 °C and 760 °C alloying components exiting solution would be observed either via the growth of carbides or as enrichment along grain boundaries.

Comparing figures 13 and 12, the dislocation density in the 0.31(2) dpa and 0.91(6) dpa FZs do not match the trend in nanohardness. A higher dislocation density in the 0.31(2) dpa sample does not translate to a higher nanohardness, and the converse for the 0.91(6) dpa sample, indicating that 1-dimensional defect density is not the only source of nanohardness. The variable that separates the two samples is dose rate, shown in table 3 the dose rate is higher in the sample with a higher damage level, though the effect on defect population in the fusion zone is not immediately clear. It may be the case that higher dimensional defect populations are able to be sustained, but speculation will remain as such until future defect population estimates in Eurofer97 are demonstrated, either through microscopy analysis or via simulation.

Irradiation, again, appears to have had little effect on nanohardness at 450 °C in all cases. Proton-induced damage relevant to hardening (loops, voids, and other defect clusters) is likely being annealed in-situ at 450 °C, as can be seen comparing both pre-heat-treated and as-welded irradiated specimens to their respective references. Existing neutron data from reactor studies at 300 °C by Lucon et al.<sup>[51]</sup> found a sharp increase in Eurofer97 irradiation hardening at a similar dpa level (hardening from yields stress measurements), indicating some intermediate temperature at which irradiation hardening is recovered. Such behaviour has been observed in another 9Cr1Mo steel, where radiation effects on yield strength at 450 °C and a neutron dose of 94 dpa are indistinguishable from the unirradiated steel,<sup>[52]</sup> further work on high-dose nanohardness at varied temperature would clarify the temperature precisely at which Eurofer97 exhibits this recovery. While the dislocation density results in this work may suggest there be no need for a post-weld heat-treatment, some small nanohardness increase remains after holding at steel operating temperature; to encourage recovery from the weld process there may have to be a post-weld heat-treatment. Given the varied microstructure retained in the weld through both irradiation temperature and post-weld heat-treatment other material properties such as creep strength may have more pronounced effects as a result. A decision on heat-treatment will have to be taken case-by-case for welds dependent on engineering requirements.

### 4.4 Application of Transient Grating Spectroscopy

From a fusion engineering perspective this result is welcome, as with dislocation population there is recovery from the as-welded condition to the state of the parent material at operating temperatures. A lack of thermal diffusivity degradation with dose is also a positive. The mobility of proton-irradiation-induced dislocations that affect electronic properties above 327 °C, established by Theodorou et al.,<sup>[48]</sup> is agreed with here by this result. As these irradiations were performed at 450 °C, defects that strongly scatter electrons will have annealed, based on this previous result. Dislocations present, and those due to proton-irradiation, are mobile at the irradiation temperature and are either being annihilated or collected around grain boundaries, carbides, voids and other larger structures. Here their scattering effects are effectively reduced: the contribution of a dislocation to the lattice disruption is minimal when compared to that already presented by the much larger microstructural

feature.

Given the sub-micron lath size the transient gratings used will have been sampling multiple laths per spot, each at a varied random orientation; some of these orientations will have included acoustic waves that were not purely SAWs; pseudo-SAWs and bulk waves can also be present that would radiate energy into the bulk. Such modes are usually excluded in single-crystal experiments but cannot be avoided here. These contributions sap energy from the transient grating excitation, prematurely in the eyes of equation 6, and falsely inflate the measured value of thermal diffusivity.

Another source of deviation in these results is the interaction of grain size and transient grating spacing, whose impact is two-fold. Firstly, large-grain or single-crystal materials are among those studied using TGS to date partly because they approximate well the continuous homogeneous medium relied upon by continuum mechanics, used to derive equation 6.<sup>[34,53]</sup> The introduction of grain boundaries and precipitates violates the homogeneity assumption, the extent and mechanism of the impact is poorly understood at present. It may be that as the scale of grains approaches that of the grating spacing the set-up of the SAW is restricted and the assumption of a uniform wave propagating outward is invalidated. Second, the thermal and elastic properties of grain boundaries are difficult to measure. When comparing single and polycrystalline thermal diffusivities there is extra electronic scattering at grain boundaries<sup>[54]</sup> that can be quantified empirically, but a qualitative analysis is not yet established. A study of pure, well-understood material, such as iron, could establish the effects of grain boundary and grain scale on thermal diffusivity readings. Generating a very fine grain structure, either through working or quenching, followed by a tempering, would yield a fine grained sample as a start point. Heat-treating the sample at a temperature suitable for controlled grain growth, and taking TGS readings in-situ would be a good measure grain effects as the grain size passes up and through the scale of the grating.

A secondary component of the SAW-grain interaction arises from the scattering and reflection of SAWs at grain boundaries. Recent FEM modelling of pure aluminium by Grabec et al.<sup>[55]</sup> shows that there is lingering surface displacement present in the wake of a single polycrystal SAW. Given the lower estimated thermal diffusivity in Eurofer97 in figure 14, there is some process driving the retention of the grating, slowing its decay. This SAW-wake may be a contributing factor. A repeat of this model for the multi-peak arrangement in TGS would shed light on the core processes happening here. Until the questions around the transition from mono- to polycrystal TGS readings have been answered, results presented herein should be treated with hesitation despite a similar trend in thermal diffusivity behaviour between TGS and LFA. Given the systematic nature of the discrepancy, relative effects remain meaningful.

The three techniques used to examine Eurofer97 in this work paint a picture of weld recovery following proton-irradiation at operating temperatures and, at least in the cases of thermal diffusivity and dislocation density, these can truly be interpreted as a recovery of thermal properties and weld-induced dislocations to the parent state. For mechanical properties, however, while nanohardness is shown to recover, desirable fine-grain and carbide structures that offer long-term structural strength and creep resistance will not have had the requisite temperature treatments in the weld. Future work should focus on weld irradiations in these key areas to continue the materials qualification process for Eurofer97.

## 5 Conclusions

As-welded and heat-treated Eurofer97 welds were examined using XRD, TGS and nanoindentation in unirradiated and 450 °C proton-irradiated states. Both thermal diffusivity and dislocation density were shown to recover to parent levels in the weld fusion zone after irradiation, indicating that at operating conditions much of the radiation damage will be annealed in-situ at low damage levels. Nanohardness saw little effect due to irradiation and, combined with thermal and dislocation results, almost all irradiation-induced damage investigated with the techniques in this work was annealed in-situ at 450 °C, with the exception being a slight enhanced thermal diffusivity recovery in the fusion zone of as-welded Eurofer97. Partial recovery of weld nanohardness was observed at 450 °C, with a complete recovery using a post-weld heat-treatment of 760 °C.

## Acknowledgements

A. P. C. Wylie would like to offer thanks to A. Wallwork for assistance with LFA experiments and A. Forrest with nanoindentation. Additional thanks to the staff at DCF for irradiation support. This work was supported by the Engineering and Physical Sciences Research Council (EPSRC), grant code EP/L01663X/1, the Henry

Royce Institute through EPSRC grants EP/R00661X/1, EP/S019367/1, EP/P025021/1 and EP/P025498/1, European Research Council (ERC) under the European Union's Horizon 2020 Research and Innovation Programme, grant code 714697.

## 6 Conflicts of Interest

The authors have no interests to disclose.

## 7 Data Availability

The data that support the findings of this study are openly available in an online repository, DOI: <https://zenodo.org/record/7580024>

## References

- [1] G. S. Was, Z. Jiao, E. Getto, K. Sun, A. M. Monterrosa, S. A. Maloy, O. Anderoglu, B. H. Sencer, and M. Hackett, *Scripta Materialia*, 2014, **88**, 33–36.
- [2] G. Federici et al., *Nucl. Fusion*, 2017, **57**, 1–26.
- [3] J. H. You and G. Mazzone, *Fusion Engineering and Design*, 2016, **109-111**, 1598–1603.
- [4] Y. Poitevin, I. Ricapitoa, and M. Zmitko, *Fusion Engineering and Design*, 2014, **89**, 1113–1118.
- [5] K. Keogh, S. Kirk, W. Suder, I. Farquhar, T. Tremethick, and A. Loving, *Fusion Engineering and Design*, 2018, **136**(A), 461–466.
- [6] B. Van der Schaaf et al., *Fusion Engineering and Design*, 2003, **69**, 197–203.
- [7] P. Fernández, A. M. Lancha, J. Lapeña, and M. Hernández-Mayoral, *Fusion Engineering and Design*, 2001, **58**, 787–792.
- [8] Y. Poitevin, P. Aubert, E. Diegele, G. De Dinechin, J. Rey, M. Rieth, E. Rigal, A. Von Der Weth, J. L. Boutard, and F. Tavassoli, *Journal of Nuclear Materials*, 2011, **417**, 36–42.
- [9] P. Aubert, F. Tavassoli, M. Rieth, E. Diegele, and Y. Poitevin, *Journal of Nuclear Materials*, 2011, **417**, 43–50.
- [10] S. Kirk, W. Suder, K. Keogh, T. Tremethick, and A. Loving, *Fusion Engineering and Design*, 2018, **136**(A), 612–616.
- [11] J. Konys and W. Krauss, *Journal of Nuclear Materials*, 2013, **442**(1-3), S576–S579.
- [12] J. Konys, W. Krauss, H. Steiner, J. Novotny, and A. Skrypnik, *Journal of Nuclear Materials*, 2011, **417**(1-3), 1191–1194.
- [13] C. A. Dennett and M. P. Short, *Journal of Applied Physics*, 2018, **123**(215109), 1–9.
- [14] A. Reza, C. A. Dennett, M. P. Short, J. Waite, Y. Zayachuk, C. M. Magazzini, S. Hills, and F. Hofmann, *Review of Scientific Instruments*, 2020, **91**(054902).
- [15] A. Reza, H. Yu, K. Mizohata, and F. Hofmann, *Acta Materialia*, 2020, **193**, 270–279.
- [16] A. Reza, Y. Zayachuk, H. Yu, and F. Hofmann, *Scripta Materialia*, 2020, **174**, 6–10.
- [17] F. Hofmann, M. P. Short, and C. A. Dennett, *MRS Bulletin*, 2019, **44**(5), 392–402.
- [18] E. Gaganidze, F. Gillemot, I. Szenthe, M. Gorley, M. Rieth, and E. Diegele, *Fusion Engineering and Design*, 2018, **135**, 9–14.
- [19] K. Haarman, J. C. Vaillant, B. Vandenberghhe, W. Bendick, and A. Arbab, *The T91/P91 Book*, Vallourec and Mannesmann Tubes, 2 ed., 2008.
- [20] L. K. Mansur, *Journal of Nuclear Materials*, 1993, **206**(2-3), 306–323.

- [21] G.S.Was, *Fundamentals of Radiation Materials Science*, Springer, 2 ed., 2007.
- [22] H. Miura, S. Satoh, M. Enoeda, T. Kuroda, H. Takatsu, Y. Kawamura, and S. Tanaka Design of Test Blanket System for ITER Module Testing Technical report, Japan Department of Fusion Engineering Research, 1997.
- [23] N. Baluc, R. Schäublin, P. Späti, and M. Victoria, *Nuclear Fusion*, 2004, **44**(1), 56.
- [24] F. Ditrói, F. Tárkányi, J. Csikai, M. S. Uddin, M. Hagiwara, and M. Baba In *AIP Conference Proceedings*, Vol. 769, pp. 1011–1014, 2005.
- [25] N. Soppera, E. Dupont, and M. Bossant JANIS Book of proton-induced cross-sections Technical report, Nuclear Energy Agency, 2012.
- [26] R. Stoller, M. Toloczko, G. Was, A. Certain, and S. Dwaraknath, *Nuclear Instruments and Methods in Physics Research B*, 2013, **310**, 75–80.
- [27] B. L. Henke, E. M. Gullikson, and J. C. Davis, *Atomic Data and Nuclear Data Tables*, 1993, **54**(2), 181–342.
- [28] P. M. Giles, M. H. Longenbach, and A. R. Marder, *Journal of Applied Physics*, 1971, **42**(11), 4295.
- [29] G. Ribárik, B. Jóni, and T. Ungár, *Accepted in J. Mater. Sci. Technol.*, 2019, **35**(7), 1508–1514.
- [30] T. Ungár, J. Gubicza, G. Ribárik, and A. Borbély, *Journal of Applied Crystallography*, 2001, **34**(3), 298–310.
- [31] M. A. Krivoglaz, *X-Ray and Neutron Diffraction in Nonideal Crystals*, Springer, Berlin, 1 ed., 1996.
- [32] M. Wilkens, *Physica Status Solidi (a)*, 1970, **2**(2), 359–370.
- [33] C. A. Dennett and M. P. Short, *Applied Physics Letters*, 2017, **110**(21), 211106.
- [34] O. W. Kading, H. Skurk, A. A. Maznev, and E. Matthias, *Appl. Phys. A*, 1995, **61**, 253–261.
- [35] C. A. Dennett and M. P. Short, *Journal of Applied Physics*, 2018, **123**(215109), 1 – 9.
- [36] R. A. Duncan, F. Hofmann, A. Vega-Flick, J. K. Eliason, A. A. Maznev, A. G. Every, and K. A. Nelson, *Applied Physics Letters*, 2016, **109**(15), 151906.
- [37] L. Vozar and W. Hohenauer, *High Temperatures - High Pressures*, 2003, **35-36**, 253–264.
- [38] W. Oliver and G. Pharr, *Journal of Materials Research*, 1992, **7**(6), 1564–1583.
- [39] W. C. Oliver and G. M. Pharr, *Journal of Materials Research*, 2004, **19**(1), 3–20.
- [40] V. B. Oliveira, K. D. Zilnyk, and H. R. Sandim, *Journal of Phase Equilibria and Diffusion*, 2017, **38**(3), 208–216.
- [41] H. Bhadeshia and R. Honeycombe in *Steels: Microstructure and Properties*; Elsevier, Boston, 2006; chapter 2, pp. 235–258.
- [42] X. Li, S. R. Holdsworth, S. Kalácska, L. Balogh, J. S. Park, A. S. Sologubenko, X. Maeder, S. Kabra, E. Mazza, and E. Hosseini, *Materials and Design*, 2021, **199**(109405).
- [43] B. Zhu, N. Leung, W. Kockelmann, S. Kabra, A. J. London, M. Gorley, M. J. Whiting, Y. Wang, and T. Sui, *Journal of Materials Science and Technology*, 2022, **114**, 249–260.
- [44] K. Mergia and N. Boukos, *Journal of Nuclear Materials*, 2008, **373**, 1–8.
- [45] G. Stornelli, A. Di Schino, S. Mancini, R. Montanari, C. Testani, and A. Varone, *Applied Sciences (Switzerland)*, 2021, **11**(22).
- [46] S. Harjo, T. Kawasaki, W. Gong, and K. Aizawa, *Journal of Physics: Conference Series*, 2016, **746**, 012046.
- [47] A. Prasitthipayong, D. Frazer, A. Kareer, M. D. Abad, A. Garner, B. Joni, T. Ungar, G. Ribarik, M. Preuss, L. Balogh, S. J. Tumey, A. M. Minor, and P. Hosemann, *Nuclear Materials and Energy*, 2018, **16**, 34–45.
- [48] A. Theodorou, Z. Kotsina, G. Apostolopoulos, M. Axiotis, A. Lagoyannis, and S. Harissopoulos, *HNPS Advances in Nuclear Physics*, 2017, **25**, 235–238.

- [49] I. Sacksteder, H. C. Schneider, and E. Materna-Morris, *Journal of Nuclear Materials*, 2011, **417**, 127–130.
- [50] E. Materna-Morris, H. C. Schneider, and A. Möslang, *Journal of Nuclear Materials*, 2014, **455**(1-3), 728–734.
- [51] E. Lucon, R. Chaouadi, and M. Decréton, *Journal of Nuclear Materials*, 2004, **69**, 373–377.
- [52] A. Alamo, J. L. Bertin, V. K. Shamardin, and P. Wident, *Journal of Nuclear Materials*, 2007, **367-370**(SPEC. ISS.), 54–59.
- [53] O. Käding, H. Skurk, and E. Matthias, *Journal de Physique IV Colloque*, 1994, **4**(C7), 7–619.
- [54] T. Gu, J. R. Medy, F. Volpi, O. Castelnau, S. Forest, E. Hervé-Luanco, F. Lecouturier, H. Proudhon, P. O. Renault, and L. Thilly, *Acta Materialia*, 2017, **141**, 131–141.
- [55] T. Grabec, I. A. Veres, and M. Ryzy, *Ultrasonics*, 2022, **119**(106585).